Neoplasia • Vol. 7, No. 3, March 2005, pp. 224–233 224

www.neoplasia.com

The Role of Heparanase in Lymph Node Metastatic Dissemination: Dynamic Contrast-Enhanced MRI of Eb Lymphoma in Mice[1]

Hagit Dafni, Batya Cohen*, Keren Ziv*, Tomer Israely*, Orit Goldshmidt†, Nava Nevo*, Alon Harmelin‡, Israel Vlodavsky§ and Michal Neeman**

*Department of Biological Regulation, The Weizmann Institute of Science, Rehovot 76100, Israel; †Department of Oncology, Hadassah-Hebrew University Hospital, Jerusalem 91120, Israel; ‡Department of Veterinary Resources, The Weizmann Institute of Science, Rehovot 76100, Israel; §Tumor and Vascular Biology Research Center, Rappaport Family Research Institute and the Bruce Rappaport Faculty of Medicine, Technion, Haifa 31096, Israel

Abstract

Heparanase expression has been linked to increased tumor invasion, metastasis, and angiogenesis and with poor prognosis. The aim of the study was to monitor the effect of heparanase expression on lymph node metastasis, in heparanase-overexpressing subcutaneous Eb mouse T-lymphoma tumors, and their draining lymph node. Dynamic contrast-enhanced magnetic resonance imaging (MRI) using biotin-BSA-GdDTPA-FAM/ROX was applied for analysis of blood volume, vascular permeability, and interstitial convection, and for detection of very early stages of such metastatic dissemination. Eb tumors increased extravasation, interstitial convection, and lymphatic drain of the contrast material. Interstitial flow directions were mapped by showing radial outflow interrupted in some tumors by directional flow toward the popliteal lymph node. Heparanase expression significantly increased contrast enhancement of the popliteal lymph node but not of the primary tumor. Changes in MR contrast enhancement preceded the formation of pathologically detectable metastases, and were detectable when only a few enhanced green fluorescent protein (EGFP)–expressing Eb cells were found near and within the nodes. These results demonstrate very early, heparanase-dependent vascular changes in lymph nodes that were visible by MRI following administration of biotin-BSA-GdDTPA-FAM/ROX, and can be used for studying the initial stages of lymph node infiltration.
Neoplasia (2005) **7,** 224–233

Keywords: Heparanase, vascular permeability, lymphatic drain, lymphangiography, MRI.

Introduction

Heparanase, an enzyme that degrades heparan sulfate proteoglycans in the extracellular matrix (ECM), was previously implicated in hematogenous metastasis and poor prognosis in a few types of cancer [1–5]. Eb mouse T-lymphoma cells are nonmetastatic, forming a defined tumor mass at the site of inoculation in nude mice. A previous study reported that Eb cells transfected to express the secreted form of heparanase acquired higher invasiveness *in vitro*, in Matrigel invasion assay, and *in vivo*, reflected by rapid and massive liver colonization [2]. The aims of the study reported here were to evaluate the role of heparanase in metastatic spread to sentinel lymph nodes, and to determine the feasibility to detect by magnetic resonance imaging (MRI) early changes associated with lymph node dissemination of metastatic tumor cells.

Early detection of dissemination of tumor cells to sentinel lymph nodes is important for evaluation of tumor progression. In particular, determination of node involvement is required for novel intervention strategies aimed at suppressing peritumor lymphangiogenesis and lymphatic drain [6–8]. A number of imaging modalities were used for the detection of lymph node involvement including lymphoscintigraphy [9] and MRI [10–14]. Ultrasmall superparamagnetic iron oxide particles (USPIO) and gadolinium-labeled molecules were used for intravenous and interstitial MR lymphography, and revealed changes in lymph nodes when those exhibited substantial tumor involvement. Long-circulating USPIO accumulate in lymph nodes by direct passage through capillaries, or by exit from the circulation to the interstitium and drain through lymphatic vessels [15,16]. Within 24 hours from intravenous injection, endocytosis of USPIO by macrophages in the nodes causes a decrease in signal intensity due to magnetic susceptibility and T2-shortening effects. Recently, USPIO showed high sensitivity and specificity for detection of lymph node

Abbreviations: MRI, magnetic resonance imaging; MR, magnetic resonance; BSA, bovine serum albumin; GdDTPA, gadolinium–diethylene triamine pentaacetic acid; TR, repetition time; TE, echo time; FOV, field of view; fBV, blood volume fraction; PS, permeability surface area product; MIP, maximal intensity projection; 3D-GE, three-dimensional gradient echo; EGFP, enhanced green fluorescent protein; ECM, extracellular matrix; USPIO, ultrasmall superparamagnetic iron oxide particles; ΔSI, difference in signal intensity; SNR, signal-to-noise ratio; VEGF, vascular endothelial growth factor; bFGF, basic fibroblast growth factor

Address all correspondence to: Michal Neeman, Department of Biological Regulation, The Weizmann Institute of Science, Rehovot 76100, Israel. E-mail: michal.neeman@weizmann.ac.il

[1]This work was supported by research grants from the Willner Center for Vascular Biology (to M.N.) and by the USA NIH RO1 CA90471 (to M.N. and Prof. Zaver Bhujwalla; Johns Hopkins).
Received 26 June 2004; Revised 1 August 2004; Accepted 6 August 2004.

DOI 10.1593/neo.04433

metastases in a clinical trial [16]. Tumor involvement is detected by exclusion of the contrast material from tumor-colonized lymph nodes. Thus, this method does not measure the drain from the primary tumor toward the lymph node, and is also not sensitive to early stages of metastasis when the tumor burden in the node is very low.

Interstitial MR lymphography was done using contrast materials that vary in size and nature [10–12,17]. Recently, gadolinium-labeled dendrimers of various generation and core type were used for visualizing lymphatic vessels and lymph nodes in normal mice and in pathologies such as lymphangitis, lymphoma, and lymph node metastases [18]. Lymphangiography by this approach cannot map the flux of peritumor interstitial convection because the pattern of lymphatic drain that is detected is dictated by the site of administration of the contrast agent.

Albumin-GdDTPA, a prototype of macromolecular MR contrast materials [19], was first reported in 1987 [20]. Although Albumin-GdDTPA is not a candidate for clinical application due to slow and incomplete clearance and potential induction of immunologic toxicity [19], it was used extensively in many experimental tumor models [21–24]. Blood volume and microvascular permeability were quantitatively estimated using kinetic models and correlated with histologic capillary density [22,25,26]. In addition, the macromolecular contrast material was biotinylated to allow histologic detection of its distribution [27].

We used similar contrast materials, albumin triply labeled with biotin, fluorescent tag, and GdDTPA (biotin-BSA-GdDTPA-FAM/ROX), to study the microvasculature of normal and malignant tissues [28–33]. The application of this contrast material was further extended by demonstrating interstitial convection and lymphatic uptake of the extravasated contrast material, which was detectable by MRI and *ex vivo* confocal microscopy [28,29].

We show here that MRI and histology revealed elevated vascular permeability in lymphoma tumors as well as in their draining lymph nodes. Interstitial flow maps showed directional drain of the contrast agent from the primary tumor, whereas contrast enhancement in the lymph nodes occurred before the formation of liver metastases and preceded pathologically detectable lymphatic metastasis. Heparanase expression induced significant increases in MR contrast enhancement of the popliteal lymph node, suggesting that heparanase may support secondary angiogenesis during tumor cell colonization of the nodes. Hence, a single administration of biotin-BSA-GdDTPA-FAM/ROX provided a tool for evaluation of the very early stages of lymphatic-mediated tumor metastasis.

Materials and Methods

Contrast Materials

Biotin-BSA-GdDTPA was derived from bovine serum albumin (BSA) labeled with biotin and GdDTPA (biotin-BSA-GdDTPA; approximately 82 kDa; relaxivity of 192 mM^{-1} s^{-1} at 4.7 T) [30]. BSA and biotin-BSA-GdDTPA were further labeled with rhodamine (ROX) or fluorescein (FAM) derivatives (Molecular Probes, Inc., Eugene, OR) [30]. During the MRI session, biotin-BSA-GdDTPA was injected intravenously (10 mg/mouse, out of which 2.5 mg was also fluorescently labeled). Immediately after imaging, BSA labeled with the other fluorescent marker (3 mg/mouse) was administered intravenously, the mice were sacrificed within 3 minutes, and tissues were retrieved for histologic analysis.

Cell Lines and Tumor Models

Eb mouse T-lymphoma cells transfected with chicken heparanase (Eb-chk-hpa) or mock-transfected (Eb-mock) were cultured as reported [2,34]. Stably transfected cells were maintained in selection medium containing neomycin (400 μg/ml; Gibco BRL, Life Technologies, Paisley, Scotland, UK). Heparanase activity was verified as reported previously [35,36].

Heparanase and mock-transfected Eb cells (3×10^5) were further stably transfected with enhanced green fluorescent protein (EGFP; pIRES-EGFP-Puro plasmid; 2 μg) using the FuGene 6 reagent, according to manufacturer procedure (Roche Diagnostics Corporation, Mannheim, Germany). Stable Eb cell populations expressing various EGFP levels were selected in the presence of 2.5 μg/ml puromycin (Sigma Chemical Co., St. Louis, MO).

All animal experiments were approved by the Weizmann Institutional Animal Care and Use Committee. CD1-nude mice (female; 6–10 weeks old; body weight ~30 g) were inoculated with tumor cells (0.5×10^6 cells/mouse) in the subcutaneous/intradermal tissue of the hind limb.

In Vivo MRI Experiments

Mice were studied by MRI 8 days after inoculating the tumor cells (Eb-chk-hpa, $n = 19$; Eb-mock, $n = 10$). Mice were anesthesized by intraperitoneal injection of 75 mg/kg ketamine (Fort Dodge Animal Health, Fort Dodge, IA) and 3 mg/kg xylazine (Vitamed Ltd., Bat-Yam, Israel) and half of the initial dose was added subcutaneously, 20 minutes later, in order to prolong the anesthesia. The tail vein was catheterized with home-built catheters fitted with heparin-washed needle. MRI experiments were performed at 4.7 T on a horizontal Bruker Biospec spectrometer (Karlsruhe, Germany) using a 7-cm resonator for excitation and an actively decoupled 1.5-cm surface coil for detection. Three-dimensional gradient echo (3D-GE) images of the tumor-bearing limb were acquired before and sequentially for 55 minutes after intravenous injection of biotin-BSA-GdDTPA. The three-dimensional field of view (FOV) of the image covered the entire hind limb up to the pelvis, containing the tumor and the popliteal lymph node.

Experimental parameters: precontrast flip angles 5°, 15°, 30°, 50°, 70°; postcontrast flip angle 15°; TR 10 milliseconds; TE 3.6 milliseconds; two averages; spectral width 50,000 Hz; matrix $128 \times 128 \times 64$; acquisition time 163 seconds; frequency encoding direction head–foot, FOV $20 \times 20 \times 20$ mm; slice thickness 312 μm; in-plane resolution 156×156 μm.

Analysis of Dynamic MR Data

The 3D datasets were zero-filled to 128 × 128 × 128. Maximal intensity projections (MIPs) were generated for each postcontrast time point, after subtraction of the precontrast dataset (Figure 1). Presentation of 3D images as MIP highlights regions with pronounced contrast enhancement. The diameter of intratumor vessels and normal capillaries is smaller than the image resolution (~150 μm) and, due to partial volume averaging, the contribution of these vessels is less pronounced relative to the larger vessels observed in the MIPs early after injection of contrast material. However, vessel density and regions of permeable vessels were extracted from the 3D datasets by pharmacokinetic analysis of the accumulation of contrast material. Pixel-by-pixel analysis was done on a personal computer using MATLAB software (MathWorks, Inc., Natick, MA) to generate concentration maps of biotin-BSA-GdDTPA for selected slices of the GE-3D datasets as described [33]. Precontrast longitudinal relaxation rate (R_{1pre}) maps were derived from the variable flip angle data by nonlinear best fit to Eq. (1):

$$I = \frac{M_0 \sin\alpha(1 - e^{-TR R_{1pre}})}{1 - \cos\alpha e^{-TR R_{1pre}}} \quad (1)$$

where I is signal intensity as a function of pulse flip angle α, TR is the repetition time (10 milliseconds), and the preexponent term M_0 includes the spin density and the T_2 relaxation, which are assumed to be constant.

Postcontrast R_1 values (R_{1post}) were calculated from precontrast and postcontrast 3D-GE signal intensities (Eq. (2)):

$$\frac{I_{pre}}{I_{post}} = \frac{M_0 \sin\alpha(1 - e^{-TR R_{1pre}})/(1 - \cos\alpha e^{-TR R_{1pre}})}{M_0 \sin\alpha(1 - e^{-TR R_{1post}})/(1 - \cos\alpha e^{-TR R_{1post}})} \quad (2)$$

Finally, concentration maps were calculated based on the relaxivity R of biotin-BSA-Gd-DTPA [192 $mM^{-1} s^{-1}$; Eq. (3)]:

$$[\text{biotin} - \text{BSA} - \text{GdDTPA}] = \frac{1}{R}(R_{1post} - R_{1pre}) \quad (3)$$

Blood concentration was evaluated from early concentration maps of slices containing the femoral vein. The change in concentration postcontrast was used for the derivation of three parameter maps [28] (Figure 2):

1. The blood volume fraction (fBV): the ratio between the extrapolated concentration of biotin-BSA-GdDTPA at the time of administration and the concentration in the blood. This parameter indicates (micro)vascular density.
2. The permeability surface area product (PS; min^{-1}): the initial rate of contrast accumulation (first 15 minutes postcontrast) normalized to initial blood concentration (1.5 minutes postcontrast). PS reflects the leak of macromolecules out of blood vessels and their accumulation in the tissues.
3. Macromolecular convection (Time2Max, min): the time at which the rate of accumulation of biotin-BSA-GdDTPA was maximal. Postcontrast time was divided into six semioverlapping intervals of six scans (16 minutes and 18 seconds each) and, for each interval, the linear slope was derived.

Numeric values of fBV and PS were calculated from mean concentration values at selected regions of interest in all relevant slices (concentration maps) containing the tumor or the popliteal lymph node. For presentation of parametric maps, the stacks of fBV and PS maps (generated for slices of interest) were projected to show the mean value in each pixel in the axial plain. Time2Max maps were projected to show the earliest time of maximal rate of accumulation in each pixel. Before projecting, linear slopes with $r < 0.7$ (for node slices) or $r < 0.9$ (for tumor slices) were discarded. Note that no threshold was used for derivation of numeric values from regions of interest, as listed above.

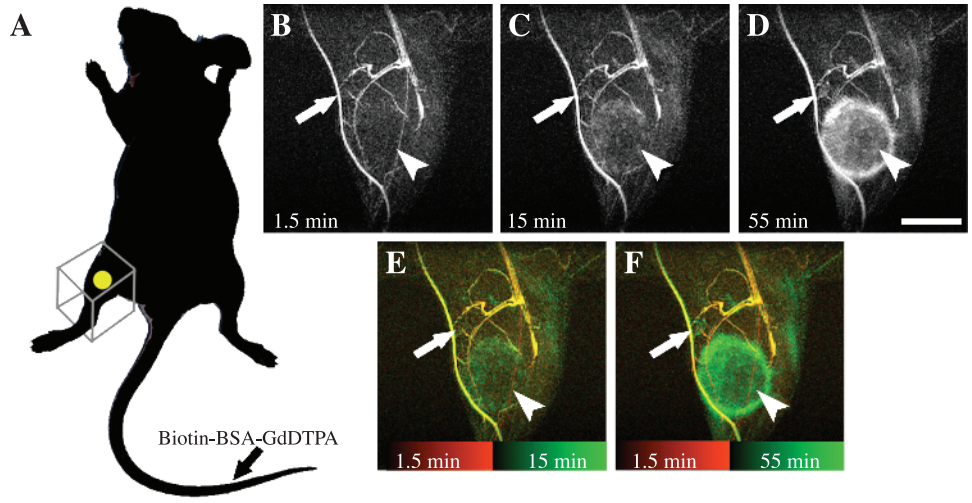

Figure 1. *Dynamic contrast-enhanced MRI. Tumor-bearing mice were studied before and after intravenous injection of macromolecular contrast material (Biotin-BSA-GdDTPA) in the tail vein. Dynamic 3D imaging included follow-up of contrast enhancement for 1 hour postcontrast (20 time points). (A) Tumor inoculation site (yellow spot) and the FOV of the image (framed box) are indicated. (B–D) Maximal intensity projections of selected 3D images of Eb-chk-hpa tumor-bearing mouse (1.5, 15, and 55 minutes postcontrast). (E and F) Overlay of the maximal intensity projections. Early time point in red and later time points in green. Arrows indicate the popliteal lymph node; arrowheads point the tumor. Scale bar = 5 mm.*

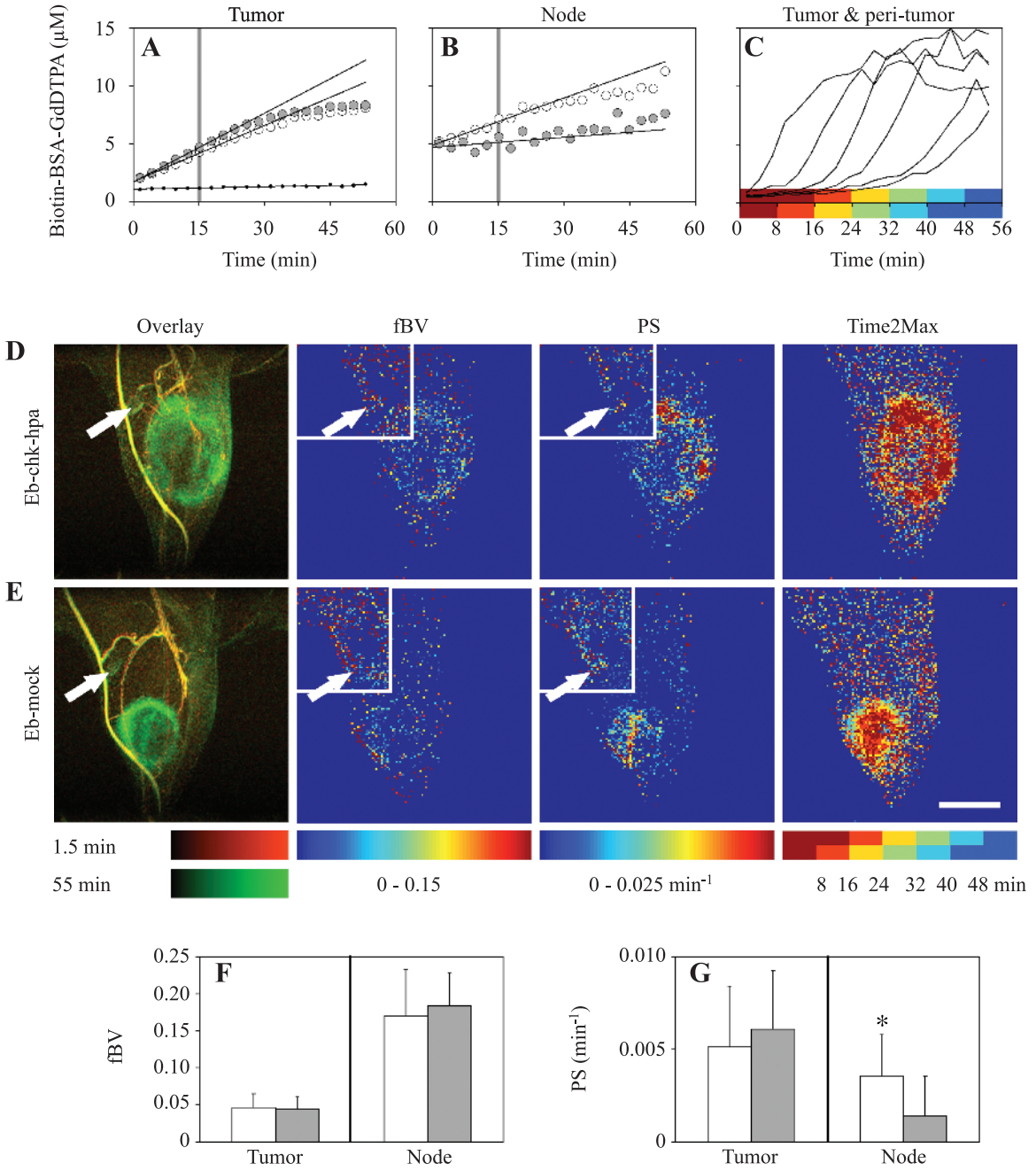

Figure 2. *Blood volume, vascular permeability, and interstitial flow of primary Eb tumors and draining lymph nodes. (A and B) Typical concentration curves for tumor region and popliteal lymph node of mice inoculated with Eb-chk-hpa (white circles) or Eb-mock (gray circles) tumors and for normal tissue away from the tumor (black dots). Linear fit of the first 15 minutes (trend lines) was used for derivation of blood volume fraction (fBV; tissue concentration at time zero divided by blood concentration) and permeability surface area product (PS; the slope of concentration curve normalized to blood concentration). (C) Contrast accumulation curves of different tumor and peritumor regions. Color-coded semioverlapping time intervals of delayed accumulation of contrast material used for mapping interstitial flow (Time2Max). (D and E) Representative overlay MIPs (1.5 minutes in red; 55 minutes in green), fBV, PS, and Time2Max map 8 days after inoculation of tumors. Tumor slices, large frame; popliteal slices, small frame. Arrows indicate the popliteal lymph node. Scale bar = 5 mm. (F and G) fBV and PS values were calculated for each mice by linear regression, after averaging the concentration of contrast material in the selected regions of interest (tumor or popliteal lymph node) from all relevant concentration maps. Values (mean ± SD) for Eb-chk-hpa (white bars; n = 19) and Eb-mock (gray bars; n = 10). *Indicates two-tailed unpaired t test (P = .02).*

In addition, maps of *flow direction* were generated. The signal intensity of the first time point (showing only vascular enhancement) was subtracted from all subsequent time points (showing vascular and extravascular signal), so as to eliminate the contribution of blood vessels to the MIPs. After subtraction, MIPs were generated for those image slices including the tumor. Flow vectors were calculated from the local signal intensity gradient (ΔSI and direction) for each pixel in the MIP (calculated in 3 × 3 matrix; for pixels with SNR >12 times mean SD of the noise). ΔSI was summed in each time interval (16 minutes, 18 seconds each) such that random fluctuations were largely averaged. Finally, the

corresponding pixel in the flow map was assigned the angle (direction of intensity gradient in an arbitrary axis system, encoded by color) obtained at the time interval with the highest-magnitude change (see Results section for more details and graphic representations of flow analysis).

Confocal Microscopy and Histology

Tumors, lymph nodes (popliteal and subiliac), and livers were excised for histology on day 8 from most mice studied by MRI and from mice with EGFP-labeled Eb tumors (Eb-chk-hpa, $n = 3$; Eb-mock, $n = 2$). Additional tissue samples were retrieved from mice with EGFP-labeled Eb tumors on day 11 (Eb-chk-hpa, $n = 2$; Eb-mock, $n = 3$). Liver metastasis were verified 11 days after inoculation of twice the cell dose (1×10^6; Eb-chk-hpa, $n = 4$) in the lower back (instead of the hind limb) as previously described [2].

Skin and subcutaneous tumors were first scanned by confocal microscope (Eclipse TE300; Nikon, Kanagawa, Japan) equipped with laser scanning system (Radiance 2000; Bio-Rad, Hemel Hempstead, UK) [28,29]. Tissue samples were fixed in Carnoy's solution (6:3:1 ethanol/chloroform/acetic acid) embedded in paraffin and sectioned at 4 μm. Sections were deparaffinized (xylene), rehydrated (100%, 95%, 70% ethanol, and PBS; 5 minutes each), blocked (2% BSA in PBS, 1 hour), and incubated with rabbit polyclonal anti-GFP antibody (1 hour; Abcam Ltd., Cambridge, UK). Alkaline phosphatase–conjugated goat-antirabbit IgG (Jackson ImmunoResearch Laboratories, Inc., West Baltimore Pike West Grove, PA) was used as secondary antibody, with Fast Red (Sigma Chemical Co.) as a substrate for color reaction. Mayer's hematoxylin solution (Sigma Chemical Co.) was used for nuclei counterstaining.

Fluorescent contrast materials remained visible after processing for histology. Therefore, slides were only counterstained (Hoechst nuclear staining; 1:1000 in PBS for 2 minutes; Molecular Probes, Inc., Eugene, OR) and sealed with antifade reagent (Molecular Probes, Inc.). When MR contrast material was used without a fluorescent label, it was visualized using avidin FITC (Sigma Chemical Co.) or avidin Texas red (Molecular Probes, Inc.).

Fluorescent probes were viewed by Optiphot2 microscope (Nikon) and photographed by CCD camera (DVC Company, Austin, TX), and EGFP staining was examined using Eclipse E800 microscope with Digital Camera DXM 1200 (Nikon).

Results

Vascular Hyperpermeability in Primary Eb Tumors and Draining Lymph Nodes

Eb cells were inoculated in the hind limb, allowing selection of a small FOV encompassing the primary tumor and its lymphatic drain path (Figure 1). Eight days after inoculation, the primary tumor was already established, but liver metastases were not visible yet. 3D contrast-enhanced MRI was used to follow the distribution of intravenously administered macromolecular contrast material, biotin-BSA-GdDTPA, over 1 hour. Immediately after administration, the contrast material was confined to blood vessels (Figure 1*B*). During the following hour, the contrast material extravasated from leaky tumor vessels and gradually accumulated in the tumor region and in the popliteal lymph node (Figure 1, *C–F*, *arrows*). Apart from enhancing the peritumor region, within normal tissues the contrast material remained intravascular (Figure 1, *B–F*).

Blood volume fraction (fBV), indicating (micro)vascular density and permeability surface area product (PS), were extracted from the 3D dataset by pharmacokinetic analysis of the accumulation of contrast material (Figure 2, *A* and *B*; see Materials and Methods section). Eb-chk-hpa ($n = 19$) and Eb-mock ($n = 10$) tumors showed both higher blood volume and higher permeability than the normal surrounding tissues (higher fBV and PS; Figure 2). The primary tumors showed no significant difference in either fBV or PS values between Eb-chk-hpa and Eb-mock. Blood volume and permeability were also evaluated for the popliteal lymph node. Blood volume (fBV) of the popliteal lymph nodes was higher than the fBV of primary tumors. Both experimental groups showed similar fBV values of the popliteal lymph node (Figure 2*F*). Vascular permeability of the popliteal lymph node was significantly increased by heparanase expression; thus, PS was significantly higher in Eb-chk-hpa tumor-bearing mice relative to the Eb-mock group (Figure 2*G*; two-tailed unpaired *t* test, $P = .02$).

Histologic Mapping of the Distribution of Contrast Material

The distribution of contrast material was also studied by histology. Extravasation of fluorescent contrast material was found in the tumor periphery (Figure 3, *A* and *B*, *green*). Tracks of invading tumor cells were found in the periphery of primary Eb tumors (both types) with extravasated contrast material channeled along these tracks (Figure 3, *A* and *B*, *arrowheads*). In three mice, infiltrating Eb cells were also found close to the popliteal lymph node (Figure 3*C*, *arrowheads*). Inside the popliteal and subiliac lymph nodes, contrast material was detected mainly in the center and perinodal tissues (Figure 3, *C–E*). Extravasated fluorescent MR contrast material was occasionally found inside draining lymphatics (lumen diameter of approximately 100 μm) in the normal skin surrounding the tumor (Figure 3*F*). Skin lymphatics were recognized by uptake of extravasated contrast material (single-stained vessels), transparency (lack of red blood cells), and typical valve structures (Figure 3*F*, *arrowheads*).

Lymph Node Infiltration by Tumor Cells Preceded the Formation of Detectable Liver Metastases

Vascular permeability in the popliteal lymph node adjacent to primary Eb-chk-hpa tumors was significantly elevated, suggesting invasion of tumor cells into lymph nodes. Invasion of Eb cells into the normal tissues at the tumor periphery was detected, but histologic sections showed no evidence of lymph node metastases (Figures 3 and 4). To increase the sensitivity of histologic identification of single infiltrating tumor cells, Eb cells were transfected to express

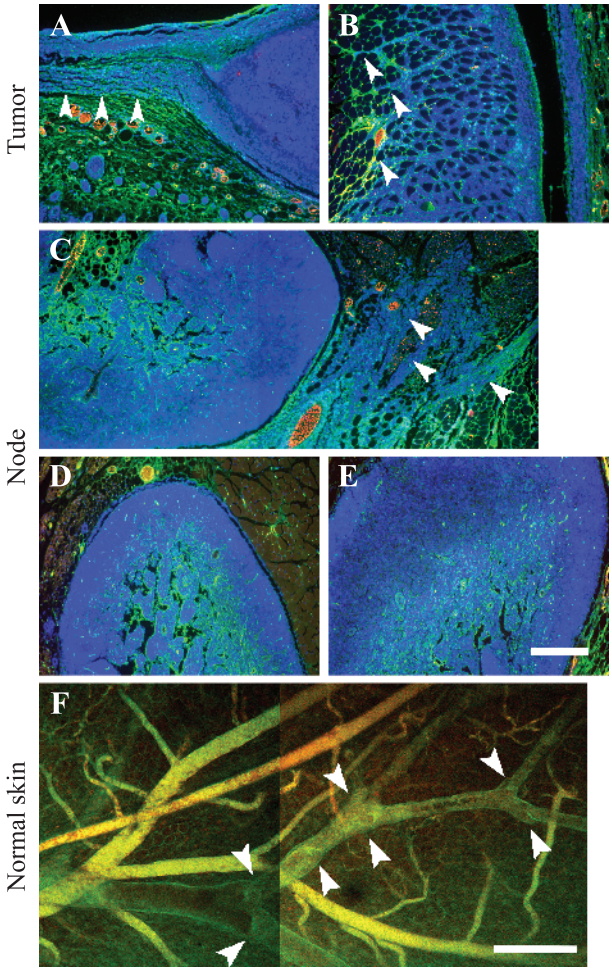

Figure 3. *Extravasation and lymphatic uptake of biotin-BSA-GdDTPA labeled with fluorescent tag [fluorescein (FAM) or rhodamine (ROX)]. The contrast material was intravenously injected and allowed to circulate for about 1 hour (displayed in green). A second probe, fluorescent-tagged BSA (ROX or FAM, respectively), was injected just before tissue retrieval (displayed in red). Blood vessels are double-stained (yellow) or more, dominated by the second probe (orange red). Extravasated contrast material in the interstitial space and inside lymphatics shows single stain (green). (A–E) Four-micrometer histologic sections counterstained for nuclei (Hoechst, Molecular Probes, Inc., Eugene, OR; blue) of tumors (day 8) and adjacent skin tissues (A and B), popliteal (C and D), and subiliac (E) lymph nodes. Arrowheads indicate contrast material along Eb cells invading the peritumor skin (A and B) and infiltrating cells close to the popliteal lymph node (C; merging of two frames). (F) Confocal microscopy of the inner side of normal skin close to the tumor (before tissue sectioning for histology; merging of two frames). Arrowheads indicate valve structures along lymphatic vessels. Scale bar = 200 μm.*

EGFP and were detected by immunohistochemistry using anti-GFP antibodies (Figure 4). Tissue sections taken 8 days after inoculation of EGFP-expressing Eb cells confirmed the invasion of tumor cells into the peritumor tissue (Figure 4, *A* and *B*). Eb cells were found in the rim of the popliteal lymph node and the subiliac lymph node (Figure 4, *C*–*F*). In addition, EGFP-expressing Eb cells were found inside blood vessels and lymphatic vessels (Figure 4, *G* and *H*). At that time (8 days), as well as 11 days after inoculation, no liver metastases could be found (Figure 4*I*). In contrast, liver metastases were detected 11 days after inoculation of twice as many (10^6) Eb-chk-hpa cells in the lower back (Figure 4*J*; as previously reported [2]). At these early time points, the number of GFP-expressing cells in the lymph nodes was too low to allow testing the impact of heparanase overexpression on the infiltration of tumor cells into sentinel lymph nodes.

Spatial Patterns of Peritumor Interstitial Drain

Vascular permeability was determined by the rate of accumulation of contrast material during the first 15 minutes postcontrast. However, the leak was continuous, generating outflow of contrast material from permeable tumor vessels and toward the peritumor tissue. Consequently, delayed enhancement was observed for the peritumor region (Figure 2*C*). Color coding the postcontrast time intervals was used to map this interstitial flow (Time2Max maps; Figure 2, *D* and *E*). These maps indicate the time of peak in accumulation rate. Elevated vascular permeability, represented by the first time interval in the Time2Max map (dark red), usually outlined the tumor. Delayed enhancement (accumulation rates that peak at later time intervals) represented regions in which enhancement was predominantly due to interstitial convection rather than vascular leak.

Vascular hyperpermeability will generate a pressure gradient that subsequently will result in a radial outward interstitial flow (convection; Time2Max running from dark red through green to blue) [28]. However, drain of contrast material in specialized fluid channels rather than (or in addition to) nonspecific percolation between cells will interrupt this well-ordered convection pattern. Fluorescence microscopy revealed lymphatic uptake and channeling of contrast material along invading tumor cells (Figure 3), supporting the existence and function of draining channels in the peritumor region. Such channels were, in some cases, large enough to be resolved also by MRI but required follow-up of individual slices of the 3D images with time (see supplementary data).

To trace the dynamic patterns of interstitial flow in the 3D MRI datasets, maps of flow direction were calculated (Figure 5; see Materials and Methods section). Tumors with outward convection showed uniform radial distribution of flow angles surrounding the tumor (Figure 5*D*), as expected from simulations (Figure 5*C*). Delayed enhancement (compare with Time2Max maps; Figure 5) was detected in some cases also directed to the tumor core, probably indicating diffusion of the macromolecular contrast material into the tumor mass. In some tumors, the radial interstitial convection was disrupted by channels that conveyed faster drain (Figure 5, *E* and *F*). Channeling of contrast material was detectable by MRI for 11/19 Eb-chk-hpa and 6/9 Eb-mock tumors. MRI-detectable peritumor channels associated with the extent of local invasion of the peritumor tissue, as detected in histologic sections, and appeared to be independent of heparanase expression.

Discussion

Heparanase (endoglycosidase) degrades heparan sulfate proteoglycans in the ECM and blood vessels wall, and thus it may promote migration and invasion of endothelial and

cancer cells [1]. In addition, release of heparan sulfate-bound growth factors [vascular endothelial growth factor (VEGF) and basic fibroblast growth factor (bFGF)] from the ECM contributes to angiogenesis, both in the primary tumor and at the site of dissemination, resulting in increased ectopic survival [1]. Nonmetastatic Eb mouse T-lymphoma cells overexpressing the secreted form of heparanase acquired increased invasiveness through reconstituted basement membrane and through tissues, manifested by rapid and massive liver infiltration, with subsequent liver metastases and dysfunction [2]. Secretion of heparanase stimulated angiogenesis and vascular maturation in these tumors was demonstrated by histology and blood oxygenation level–dependent (BOLD) contrast MRI [2].

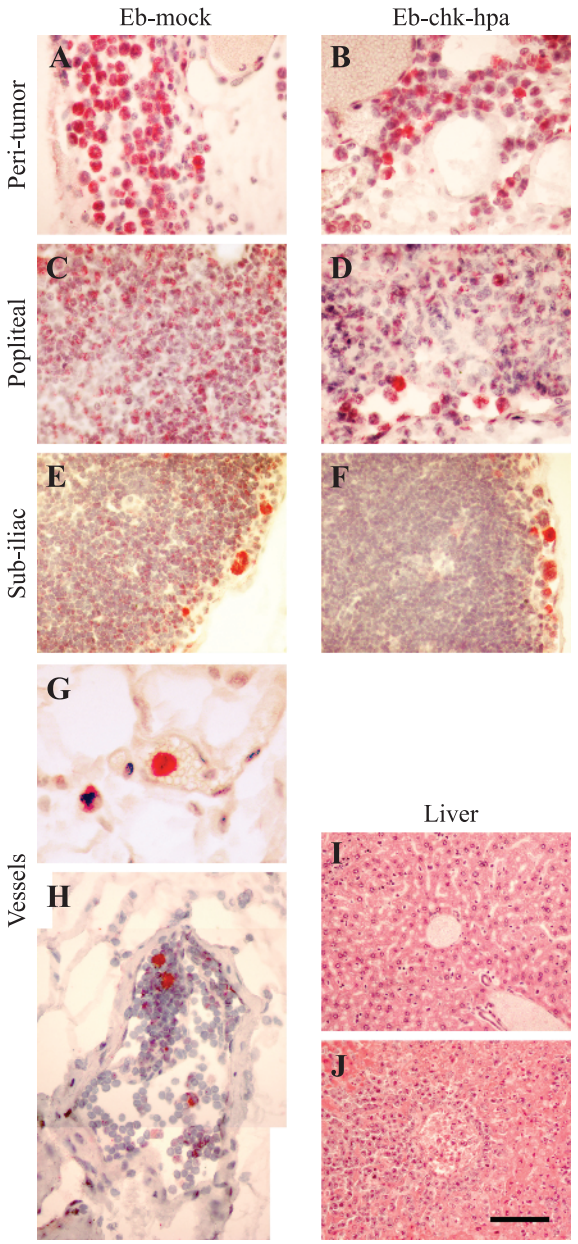

Figure 4. *Infiltration of EGFP-expressing Eb lymphoma cells into normal tissues. (A–H) EGFP-expressing cells were visualized, using anti-GFP antibody (red) and nuclear counter stain (hematoxylin), in 4-μm histologic sections obtained 8 days after inoculation in the hind limb (0.5 $\times$ 10^6 cells). Lymphoma cells were detected in the peritumor tissue (A and B), in the periphery of the popliteal (C and D) and subiliac (E and F) lymph nodes and inside blood vessels near the tumor (G; vessel filled with red blood cells), and lymphatic vessel near the subiliac lymph node (H; vessel lumen devoid of red blood cells; merging of two frames). (I and J) H&E stain of liver sections 11 days after inoculation of tumor cells in the hind limb (I; 0.5 $\times$ 10^6 cells; no metastasis) and in the lower back (J; 1 $\times$ 10^6 cells; advanced metastasis). Scale bar = 50 μm (A–F, H), 12.5 μm (G), 100 μm (I and J).*

We have recently reported that dynamic contrast-enhanced MRI, using biotin-BSA-GdDTPA, a macromolecular contrast material (a blood pool agent), can be applied for mapping of vascular permeability, interstitial convection, and lymphatic drain [28]. Acquisition of 3D gradient echo MRI allowed sampling of the entire tumor volume and comparison with the neighboring normal tissues and draining lymph nodes. As reported here, blood volume fraction (fBV) and permeability (PS) were elevated in Eb tumors relative to normal tissues, with no significant difference between heparanase and mock-transfected Eb clones. Heparanase expression increased vascular permeability in the draining lymph node; thus, PS was significantly higher in the popliteal lymph node adjacent to heparanase-expressing tumors relative to control tumors and resembled PS of the primary tumor. These results suggest that elevated PS in the lymph node might be an indication of infiltration or colonization of tumor cells into the node, resulting in increased vascular permeability as a consequence of inflammatory reaction or the release of vascular permeability factors (such as VEGF) by stroma or tumor cells.

The aim of this work was to determine whether heparanase affects the ability of lymphoma cells to take advantage of the lymphatic drainage pathway, which normally returns circulating lymphocytes (and other substances) to the blood circulation [37]. Histologic evaluation revealed that increased accumulation of contrast material in draining lymph nodes was detectable when only a few isolated EGFP-expressing tumor cells were found in the popliteal and subiliac lymph nodes, and before establishment of growing lymph node metastases. Both cell types were capable of lymph node infiltration, suggesting that Eb cells have an intrinsic ability to migrate and infiltrate the normal tissues. The intrinsic heparanase-independent motility of Eb cells was reported previously by their ability to traverse through collagen type IV, in contrast to invasion through reconstituted basement membrane, which was heparanase-dependent [2]. Heparanase expression significantly elevated nodal accumulation of contrast material, and might further facilitate colonization and shorten the time required for the formation of secondary tumor masses by affecting later stages of metastasis possibly by augmenting the angiogenic capacity of micrometastases. The number of detectable tumor cells within the nodes was too low at these early stages to allow quantitative comparison of the impact of heparanase expression on the number of tumor cells infiltrating the lymph node.

We have previously reported that VEGF-induced hyperpermeability provides a driving force for the motion of macromolecules toward draining lymphatics [28]. Hypothetically, tumor cells might take advantage of this draining current, implicating VEGF in lymph node metastasis. Increased

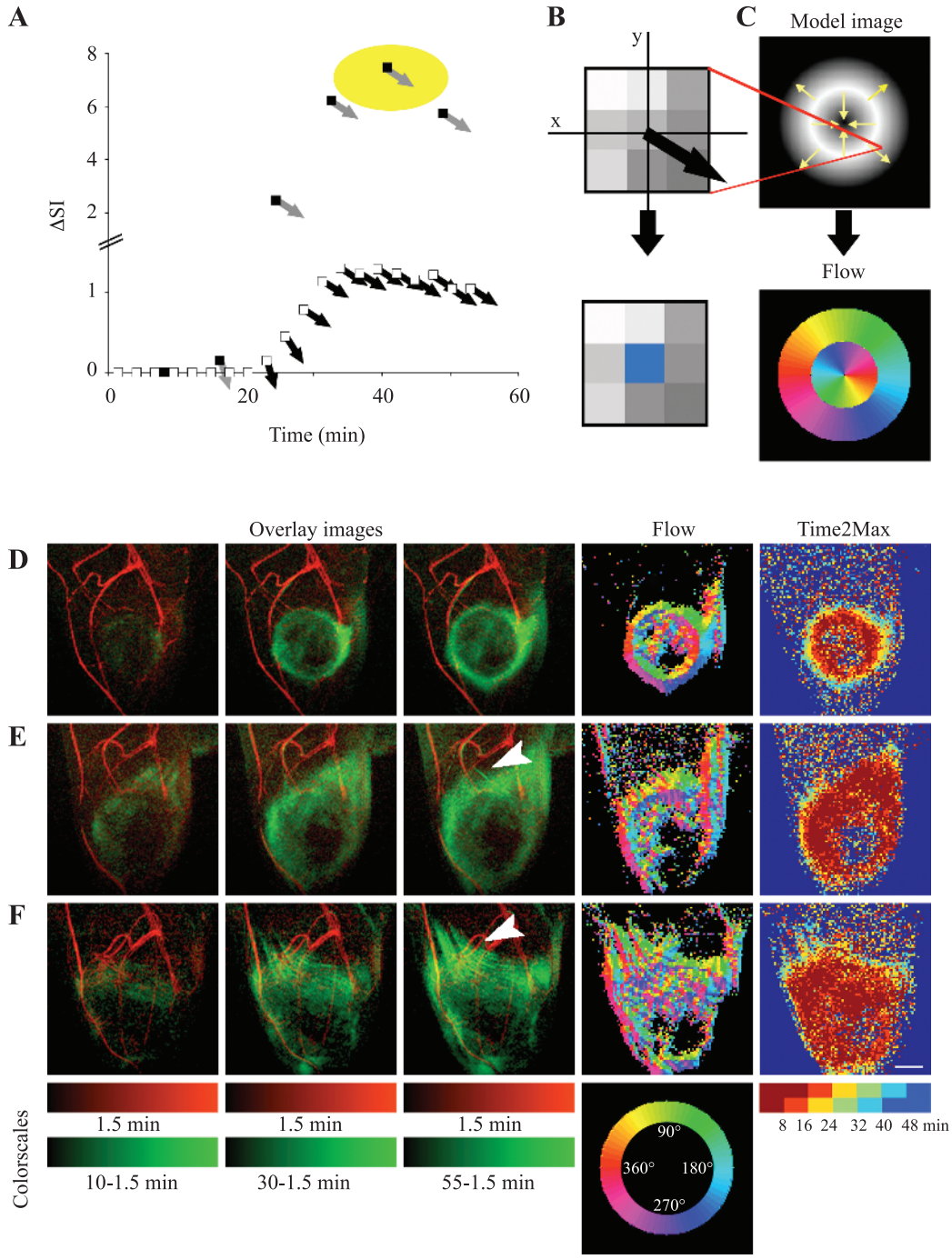

Figure 5. *Patterns of interstitial convection and flow. (A) Tracking the temporal changes in the direction of the signal intensity gradient (determined in the central pixel of 3 × 3 matrices; see Materials and Methods section). Signal intensity gradient in MIP images was assigned magnitude (ΔSI; white squares) and direction (black arrows) and then summed for each of six semioverlapping intervals (black squares, gray arrows). (B) The corresponding pixel in the flow map was assigned the angle obtained at the time interval with the highest-magnitude change (marked by yellow circle in A) color-coded with radial color scale (see below). (C) Flow analysis was simulated on a model image with inward and outward intensity gradients (indicated by arrows), resulting in a flow map. (D and F) Experimental MR datasets of three representative mice presented as overlays of MIPs of the first postcontrast time point (1.5 minutes; red) and later time points (after subtraction of the first time point; green). Arrowheads indicate draining channels. Such MIPs were used for generation of flow maps. Time2Max maps were generated from concentration maps (see Materials and Methods section). Flow maps varied from almost uniform interstitial convection (D; Eb-chk-hpa) to moderate (E; Eb-chk-hpa) and massive (F; Eb-mock) channeling of contrast material. Scale bar = 2.5 mm (see also movies in supplementary data).*

interstitial flow was recently suggested as the upstream regulator of lymphangiogenesis [38]. The time frame of our study (8 days) was significantly shorter than that required for the formation of new lymphatics in normal skin (weeks) [38,39]. Therefore, substantial peritumor lymphangiogenesis was not expected. However, our results suggest that tumor–host interaction might affect interstitial flow and lymphatic drain in the peritumor tissue. Highly efficient interstitial convection may drive macromolecules through the extracellular space without the need for specific channels. Therefore,

when interstitial flow was more effective than lymphatic drain, it resulted in almost homogeneous radial percolation flow between the cells. Such outward flux of the contrast material was also documented around VEGF-overexpressing C6 tumors [28]. However, the radial convection was disrupted when the drain of contrast material occurred more efficiently in channels. These channels might be lymphatics or other fluid channels that might form in the tissue, possibility by loosening of the ECM by the invading tumor cells or by the fluid current, as a first step in the lymphangiogenic process [38].

Both increased vascular permeability in the primary tumor and the presence of tumor cells in the sentinel lymph node can contribute to lymph node enhancement. As shown here, lymphatic drain will be manifested in the entire pathway from the primary tumor toward the lymph node as delayed enhancement. The early enhancement, during the first 15 minutes after administration of the contrast material, would be predominantly due to the effect of the tumor cells on the vasculature in their immediate proximity, and thus permeability derived for the lymph node might provide a better direct visualization of tumor cell infiltration.

So far, intravenous MR lymphangiography was done using USPIO, which, within 24 hours, slowly accumulates in normal lymph nodes, but is excluded from metastatic nodes [15]. Gadolinium-based contrast materials were used for interstitial lymphangiography [10–12,17,18]. Here we showed that dynamic contrast-enhanced MRI using a single intravenous injection of biotin-BSA-GdDTPA-FAM/ROX allowed detection of angiogenesis, vascular permeability, interstitial drain, and lymph node involvement. In contrast with USPIO, in which lymph node involvement is manifested by lack of contrast accumulation, infiltration of Eb cells into lymph nodes was manifested by increased accumulation of biotin-BSA-GdDTPA-FAM/ROX that was enhanced by heparanase expression. Lymph node infiltration was confirmed by histology and was shown to precede the formation of liver or lymph node metastases.

In summary, elevated vascular permeability in the primary Eb tumors was associated with interstitial convection and lymphatic drain of the macromolecular contrast material that was detected by MRI. Early enhancement in the lymph nodes was induced for those lymph nodes draining the primary tumors, and enhancement was further elevated for tumors overexpressing heparanase. These results further support the role of heparanase in tumor metastasis to sentinel lymph nodes, as well as the interaction between vascular permeability, interstitial pressure, and lymphatic functions, and demonstrate the ability to track these interactions by contrast-enhanced MRI.

References

[1] Vlodavsky I, Goldshmidt O, Zcharia E, Atzmon R, Rangini-Guatta Z, Elkin M, Peretz T, and Friedmann Y (2002). Mammalian heparanase: involvement in cancer metastasis, angiogenesis and normal development. *Semin Cancer Biol* **12,** 121–129.

[2] Goldshmidt O, Zcharia E, Abramovitch R, Metzger S, Aingorn H, Friedmann Y, Schirrmacher V, Mitrani E, and Vlodavsky I (2002). Cell surface expression and secretion of heparanase markedly promote tumor angiogenesis and metastasis. *Proc Natl Acad Sci USA* **99,** 10031–10036.

[3] Hulett MD, Freeman C, Hamdorf BJ, Baker RT, Harris MJ, and Parish CR (1999). Cloning of mammalian heparanase, an important enzyme in tumor invasion and metastasis. *Nat Med* **5,** 803–809.

[4] Nakajima M, Irimura T, Di Ferrante D, Di Ferrante N, and Nicolson GL (1983). Heparan sulfate degradation: relation to tumor invasive and metastatic properties of mouse B16 melanoma sublines. *Science* **220,** 611–613.

[5] Friedmann Y, Vlodavsky I, Aingorn H, Aviv A, Peretz T, Pecker I, and Pappo O (2000). Expression of heparanase in normal, dysplastic, and neoplastic human colonic mucosa and stroma. Evidence for its role in colonic tumorigenesis. *Am J Pathol* **157,** 1167–1175.

[6] Papoutsi M, Siemeister G, Weindel K, Tomarev SI, Kurz H, Schachtele C, Martiny-Baron G, Christ B, Marme D, and Wilting J (2000). Active interaction of human A375 melanoma cells with the lymphatics *in vivo*. *Histochem Cell Biol* **114,** 373–385.

[7] He Y, Kozaki K, Karpanen T, Koshikawa K, Yla-Herttuala S, Takahashi T, and Alitalo K (2002). Suppression of tumor lymphangiogenesis and lymph node metastasis by blocking vascular endothelial growth factor receptor 3 signaling. *J Natl Cancer Inst* **94,** 819–825.

[8] Stacker SA, Caesar C, Baldwin ME, Thornton GE, Williams RA, Prevo R, Jackson DG, Nishikawa Si S, Kubo H, and Achen MG (2001). VEGF-D promotes the metastatic spread of tumor cells *via* the lymphatics. *Nat Med* **7,** 186–191.

[9] Alazraki NP, Styblo T, Grant SF, Cohen C, Larsen T, and Aarsvold JN (2000). Sentinel node staging of early breast cancer using lymphoscintigraphy and the intraoperative gamma-detecting probe. *Semin Nucl Med* **30,** 56–64.

[10] Shimada M, Yoshikawa K, Suganuma T, Kayanuma H, Inoue Y, Ito K, Senoo A, and Hayashi S (2003). Interstitial magnetic resonance lymphography: comparative animal study of gadofluorine 8 and gadolinium diethylenetriamine-pentaacetic acid. *J Comput Assist Tomogr* **27,** 641–646.

[11] Ruehm SG, Corot C, and Debatin JF (2001). Interstitial MR lymphography with a conventional extracellular gadolinium-based agent: assessment in rabbits. *Radiology* **218,** 664–669.

[12] Herborn CU, Lauenstein TC, Vogt FM, Lauffer RB, Debatin JF, and Ruehm SG (2002). Interstitial MR lymphography with MS-325: characterization of normal and tumor-invaded lymph nodes in a rabbit model. *AJR Am J Roentgenol* **179,** 1567–1572.

[13] Anzai Y and Prince MR (1997). Iron oxide–enhanced MR lymphography: the evaluation of cervical lymph node metastases in head and neck cancer. *J Magn Reson Imaging* **7,** 75–81.

[14] Kobayashi H, Kawamoto S, Sakai Y, Choyke PL, Star RA, Brechbiel MW, Sato N, Tagaya Y, Morris JC, and Waldmann TA (2004). Lymphatic drainage imaging of breast cancer in mice by micro-magnetic resonance lymphangiography using a nano-size paramagnetic contrast agent. *J Natl Cancer Inst* **96,** 703–708.

[15] Weissleder R, Elizondo G, Wittenberg J, Rabito CA, Bengele HH, and Josephson L (1990). Ultrasmall superparamagnetic iron oxide: characterization of a new class of contrast agents for MR imaging. *Radiology* **175,** 489–493.

[16] Harisinghani MG, Barentsz J, Hahn PF, Deserno WM, Tabatabaei S, van de Kaa CH, de la Rosette J, and Weissleder R (2003). Noninvasive detection of clinically occult lymph-node metastases in prostate cancer. *N Engl J Med* **348,** 2491–2499.

[17] McCauley TR, Rifkin MD, and Ledet CA (2002). Pelvic lymph node visualization with MR imaging using local administration of ultra-small superparamagnetic iron oxide contrast. *J Magn Reson Imaging* **15,** 492–497.

[18] Kobayashi H, Kawamoto S, Choyke PL, Sato N, Knopp MV, Star RA, Waldmann TA, Tagaya Y, and Brechbiel MW (2003). Comparison of dendrimer-based macromolecular contrast agents for dynamic micro-magnetic resonance lymphangiography. *Magn Reson Med* **50,** 758–766.

[19] Daldrup-Link HE and Brasch RC (2003). Macromolecular contrast agents for MR mammography: current status. *Eur Radiol* **13,** 354–365 Epub 2002 October 2031.

[20] Ogan MD, Schmiedl U, Moseley ME, Grodd W, Paajanen H, and Brasch RC (1987). Albumin labeled with Gd-DTPA. An intravascular contrast-enhancing agent for magnetic resonance blood pool imaging: preparation and characterization. *Invest Radiol* **22,** 665–671.

[21] Pham CD, Roberts TP, van Bruggen N, Melnyk O, Mann J, Ferrara N, Cohen RL, and Brasch RC (1998). Magnetic resonance imaging detects suppression of tumor vascular permeability after administration

of antibody to vascular endothelial growth factor. *Cancer Invest* **16,** 225–230.

[22] Marzola P, Farace P, Calderan L, Crescimanno C, Lunati E, Nicolato E, Benati D, Degrassi A, Terron A, Klapwijk J, Pesenti E, Sbarbati A, and Osculati F (2003). *In vivo* mapping of fractional plasma volume (fpv) and endothelial transfer coefficient (Kps) in solid tumors using a macromolecular contrast agent: correlation with histology and ultrastructure. *Int J Cancer* **104,** 462–468.

[23] Wang Z, Su MY, Najafi A, and Nalcioglu O (2001). Effect of vasodilator hydralazine on tumor microvascular random flow and blood volume as measured by intravoxel incoherent motion (IVIM) weighted MRI in conjunction with Gd-DTPA-Albumin enhanced MRI. *Magn Reson Imaging* **19,** 1063–1072.

[24] Bhujwalla MZ, Artemov D, Natarajan K, Solaiyappan M, Kollars P, and Kristjansen PE (2003). Reduction of vascular and permeable regions in solid tumors detected by macromolecular contrast magnetic resonance imaging after treatment with antiangiogenic agent TNP-470. *Clin Cancer Res* **9,** 355–362.

[25] Shames DM, Kuwatsuru R, Vexler V, Muhler A, and Brasch RC (1993). Measurement of capillary permeability to macromolecules by dynamic magnetic resonance imaging: a quantitative noninvasive technique. *Magn Reson Med* **29,** 616–622.

[26] van Dijke CF, Brasch RC, Roberts TP, Weidner N, Mathur A, Shames DM, Mann JS, Demsar F, Lang P, and Schwickert HC (1996). Mammary carcinoma model: correlation of macromolecular contrast-enhanced MR imaging characterizations of tumor microvasculature and histologic capillary density. *Radiology* **198,** 813–818.

[27] Saeed M, van Dijke CF, Mann JS, Wendland MF, Rosenau W, Higgins CB, and Brasch RC (1998). Histologic confirmation of microvascular hyperpermeability to macromolecular MR contrast medium in reperfused myocardial infarction. *J Magn Reson Imaging* **8,** 561–567.

[28] Dafni H, Israely T, Bhujwalla ZM, Benjamin LE, and Neeman M (2002). Overexpression of vascular endothelial growth factor 165 drives peritumor interstitial convection and induces lymphatic drain: magnetic resonance imaging, confocal microscopy, and histological tracking of triple-labeled albumin. *Cancer Res* **62,** 6731–6739.

[29] Dafni H, Landsman L, Schechter B, Kohen F, and Neeman M (2002). MRI and fluorescence microscopy of the acute vascular response to VEGF165: vasodilation, hyper-permeability and lymphatic uptake, followed by rapid inactivation of the growth factor. *NMR Biomed* **15,** 120–131.

[30] Dafni H, Gilead A, Nevo N, Eilam R, Harmelin A, and Neeman M (2003). Modulation of the pharmacokinetics of macromolecular contrast material by avidin chase: MRI, optical, and inductively coupled plasma mass spectrometry tracking of triply labeled albumin. *Magn Reson Med* **50,** 904–914.

[31] Israely T, Dafni H, Granot D, Nevo N, Tsafriri A, and Neeman M (2003). Vascular remodeling and angiogenesis in ectopic ovarian transplants: a crucial role of pericytes and vascular smooth muscle cells in maintenance of ovarian grafts. *Biol Reprod* **68,** 2055–2064 Epub 2003 January 2022.

[32] Neeman M and Dafni H (2003). Structural, functional, and molecular MR imaging of the microvasculature. *Annu Rev Biomed Eng* **5,** 29–56.

[33] Ziv K, Nevo N, Dafni H, Israely T, Granot D, Brenner O, and Neeman M (2004). Longitudinal MRI tracking of the angiogenic response to hind limb ischemic injury in the mouse. *Magn Reson Med* **51,** 304–311.

[34] Goldshmidt O, Zcharia E, Aingorn H, Guatta-Rangini Z, Atzmon R, Michal I, Pecker I, Mitrani E, and Vlodavsky I (2001). Expression pattern and secretion of human and chicken heparanase are determined by their signal peptide sequence. *J Biol Chem* **276,** 29178–29187.

[35] Vlodavsky I (1999). Preparation of extracellular matrices produced by cultured corneal endothelial and PF-HR9 endodermal cells. Current Protocols in Cell Biology, pp. 10.14.11–10.14.14 John Wiley & Sons Inc., Hoboken, NJ.

[36] Vlodavsky I, Fuks Z, Bar-Ner M, Ariav Y, and Schirrmacher V (1983). Lymphoma cell–mediated degradation of sulfated proteoglycans in the subendothelial extracellular matrix: relationship to tumor cell metastasis. *Cancer Res* **43,** 2704–2711.

[37] Witte MH, Way DL, Witte CL, and Bernas M (1997). Lymphangiogenesis: mechanisms, significance and clinical implications. In Goldberg, EM, Rosen, EM (Eds.), Regulation of Angiogenesis, Vol. 79, pp. 65–112 Birkhauser Verlag, Basel.

[38] Boardman KC and Swartz MA (2003). Interstitial flow as a guide for lymphangiogenesis. *Circ Res* **92,** 801–808.

[39] Nagy JA, Vasile E, Feng D, Sundberg C, Brown LF, Detmar MJ, Lawitts JA, Benjamin L, Tan X, Manseau EJ, Dvorak AM, and Dvorak HF (2002). Vascular permeability factor/vascular endothelial growth factor induces lymphangiogenesis as well as angiogenesis. *J Exp Med* **196,** 1497–1506.